Proceedings of the ASME 2023 42nd International Conference on Ocean, Offshore and Arctic Engineering
OMAE2023
June 11-16, 2023, Melbourne, Australia

OMAE2023-104492

A METHODOLOGY FOR TUNING OF COMPUTATIONAL VESSEL MODELS UTILIZING WAVE MEASUREMENTS FROM X-BAND MARINE RADAR AND WAVE BUOY.

Gowtham Radhakrishnan
Department of Marine Technology,
SFI MOVE, NTNU,
Trondheim, Norway

Bernt J. Leira
Department of Marine Technology,
SFI MOVE, NTNU,
Trondheim, Norway

Zhen Gao
Department of Marine Technology,
SFI MOVE, NTNU,
Trondheim, Norway
NAOCE,SJTU,
Shanghai, China

Svein Sævik
Department of Marine Technology,
SFI MOVE, NTNU,
Trondheim, Norway

Karl E. Kaasen
Sintef Ocean
Trondheim, Norway

Konstantinos Christakos
Department of Marine Technology,
NTNU, Trondheim
MET, Bergen, Norway

Johann A. Dirdal
Department of Engineering Cybernetics, NTNU,
Trondheim, Norway

ABSTRACT

Accurate estimation of the wave field and subsequent vessel response prediction are vital for making crucial judgments on the safe and timely execution of marine operations. Decision support systems based on the Response-Based Decision-Making (RBDM) methodology are still in the early stages due to the challenges in addressing the uncertainties in the environmental conditions and vessel computational models. Therefore, this study offers a model tuning technique that utilizes the waves measured from an onboard X-band wave radar, wave buoy, and simultaneously measured vessel motions using an Inertial Measurement Unit (IMU), for applications in RBDM. For this purpose, full-scale wave and vessel response measurements were conducted using the NTNU research vessel Gunnerus on the west coast of Norway. The on-site directional wave spectra are obtained by processing the backscattered radar images using existing inversion schemes. Furthermore, the directional wave spectra are also derived from the nearby wave buoy measurements using the Maximum Entropy Method (MEM). The influential system variables in the vessel model that induce maximum variation to the response Quantities of Interest (QoIs) are quantitatively identified using probabilistic sensitivity indices. Out of the 31 system variables, only 14 were considered influential and subsequently tuned by minimizing the error between the measured and simulated response spectra. Heave, roll, and pitch modes were tuned and results exhibit superior agreement with the measured response spectra.

Keywords: Model tuning, X-band wave radar, Wave Buoy, Maximum Entropy Method, Sensitivity Study

NOMENCLATURE

RBDM	Response-Based Decision Making
FFT	Fast Fourier Transform
MEM	Maximum Entropy Method
CoG	Center of Gravity
CO	Center of Waterplane area
CM	Center of Measurement axis
Xcg	Longitudinal coordinate of CoG
Ycg	Transverse coordinate of CoG
Zcg	Vertical coordinate of CoG
M	Vessel Mass at CO
I_{44}	Roll moment of Inertia at CO
I_{55}	Pitch moment of Inertia at CO
I_{66}	Yaw moment of Inertia at CO

B_{33}^{v} Additional heave damping coefficient at CO
B_{44}^{v} Additional roll damping coefficient at CO
B_{55}^{v} Additional pitch damping coefficient at CO
$B_{33,cr}^{v}$ Critical heave damping at CO
$B_{44,cr}^{v}$ Critical roll damping at CO
$B_{55,cr}^{v}$ Critical pitch damping at CO
St_{33}^{e} External heave stiffness at CO
St_{44}^{e} External roll stiffness at CO
St_{55}^{e} External pitch stiffness at CO
Am_{11}^{e} External surge added mass coefficient at CO
Am_{22}^{e} External sway added mass coefficient at CO
Am_{33}^{e} External heave added mass coefficient at CO
Am_{44}^{e} External roll added mass coefficient at CO
Am_{55}^{e} External pitch added mass coefficient at CO
Am_{66}^{e} External yaw added mass coefficient at CO
Fr_{1}^{e} External real surge excitation coefficient at CO
Fi_{1}^{e} External imaginary surge excitation coefficient at CO
Fr_{2}^{e} External real sway excitation coefficient at CO
Fi_{2}^{e} External imaginary surge excitation coefficient at CO
Fr_{3}^{e} External real heave excitation coefficient at CO
Fi_{3}^{e} External imaginary heave excitation coefficient at CO
Fr_{4}^{e} External real roll excitation coefficient at CO
Fi_{4}^{e} External imaginary roll excitation coefficient at CO
Fr_{5}^{e} External real pitch excitation coefficient at CO
Fi_{5}^{e} External imaginary pitch excitation coefficient at CO
Fr_{6}^{e} External real yaw excitation coefficient at CO
Fi_{6}^{e} External imaginary yaw excitation coefficient at CO

1. INTRODUCTION

The presence of harsh environmental conditions poses a major challenge to the safe execution of marine operations. The traditional practice to estimate the weather window and limiting criteria for marine operations is through characteristic parameters of the environmental conditions. Contrastingly, setting limiting criteria based on the responses, also known as Response-Based Decision Making (RBDM), can facilitate superior decision-making for different kinds of marine operations. However, the realization of RBDM in a vessel's onboard system is still at its early stage due to the challenges in addressing the uncertainties in the vessel computational model and the estimation of incoming wave conditions. Therefore, the proposed study aims to minimize the system uncertainties by tuning the computational vessel models in presence of measured waves and vessel responses. The tuned models can, then, be applied to the RBDM process. The technique is illustrated using the full-scale measurement campaign conducted using the Research Vessel (R/V) Gunnerus along the west coast of Norway.

The tuning of vessel system parameters requires precise wave conditions at the site as input. Usually, the weather service providers issue forecasted wave spectra from phase-averaged models on a Global grid. However, such wave modeling is usually associated with uncertainties. Therefore, a wave measurement technique must be employed for a precise determination of waves at the site. Waves can be measured on-site by directly employing in-situ devices or measured remotely using remote-sensing techniques. The in-situ devices include wave-rider buoys – *heave-roll-pitch*, pressure sensors, etc. These devices measure the wave elevation, wave slopes, horizontal displacements, etc., from which a 1-Dimensional (1-D) spectrum can be obtained [1]. Additionally, directional wave spectra can also be estimated using Maximum Likelihood Estimation (MLM), or by means of the Maximum Entropy Method (MEM) [2]. Waves can be measured along the satellite footprint using Synthetic Aperture Radars (SAR). SAR images can then be processed to retrieve the directional spectra [3]. Coherent or Non-coherent wave radars, positioned on top of a vessel or platform, can measure incoming waves [4]. Furthermore, the High-Frequency (HF) radars positioned along the coasts can be employed for the estimation of wave and current conditions [5]. The operational site, ease of deployment, and the available budget greatly determine the choice of a particular measurement technique.

Once the true wave conditions at the site are measured, the computational system parameters are tuned using the measured vessel responses. Of the considered 31 system parameters, only some of them influence the responses to a great extent. Such influential parameters are identified through a probabilistic sensitivity study. Radhakrishnan et al. [6] investigated the sensitivity of the response RMS to parametric variations. Further, Radhakrishnan et al. [7] identified that the CoG and viscous Roll damping coefficient are influencing the Roll response considerably, and subsequently tuned those parameters using measurements from an operational offshore vessel. The sensitivity study was conducted with only 10 system variables in those studies. However, in the present study, the sensitivity of the objective function is analyzed considering 31 system variables, and the influential variables are calibrated using simultaneous wave and response measurements.

The paper is organized as follows: Sec. 2 describes the full-scale experiments conducted in the vicinity of Ålesund, and procedures for deriving the directional spectra from in-situ measurement devices. Further, the theoretical background on vessel hydrodynamic analysis and computational model tuning is presented. Sec. 3 introduces the practical implementation procedures in model tuning. The results of the probabilistic sensitivity study and the tuning results are presented and discussed in Sec. 4. Brief conclusive statements are given in the final section.

2. THEORY AND METHODOLOGY

2.1 Full-Scale Experiments

In the Breisundet strait, located on the west coast of Norway, full-scale measurements were carried out to measure the waves and ship motions simultaneously. The tests were conducted close to a SEAWATCH Wavescan (*heave-roll-pitch*) buoy. The heave, compass, pitch, and roll buoy data is publicly available via the Thredds Service at the Norwegian Meteorological Institute [8]. The test and the buoy locations are

shown in Fig. 1. The vessel is located at a distance of around ~545 m from the buoy.

FIGURE 1: LOCATION OF THE VESSEL (YELLOW MARKER) AND BUOY D (GREEN MARKER) AT BREISUNDET SHOWN USING GOOGLE EARTH.

An X-band wave radar provided by Miros was installed on the R/V Gunnerus in order to measure the waves. The rotating wave radar produces a sequence of backscattered image discs every ~2.45 seconds. The vessel motions were measured using a SeaPath 200 Inertial Measurement Unit (IMU) with a sampling frequency of 10 Hz. At Breisundet, the vessel was kept at 4 different headings relative to the incoming dominant wave direction. The vessel was positioned for about 40 minutes at each heading angle using thrusters, and the waves and ship motions were measured simultaneously. Table 1 list the experimental details. Since the Captain positioned the vessel based on visual judgment, there could be $\pm$ 5-10 deg errors associated with the relative wave heading. Only a part of the experimental data collected at Breisundet was utilized in this study while other test data collected in Sulafjorden and at Frøya were not utilized. The test data collected at Breisundet was considered highly important since both local wind seas and swell coming from the open ocean were present.

TABLE 1: FULL-SCALE EXPERIMENTS CONDUCTED ON 03-04-2022 FOR 4 DIFFERENT HEADINGS

	Start Time (UTC)	End Time (UTC)	Relative Heading
Case 1	07:12:00	07:55:00	~0 deg
Case 2	08:00:00	08:38:00	~30 deg
Case 3	08:39:00	09:19:00	~60 deg
Case 4	10:00:00	10:20:00	~90 deg

2.2 Measurement techniques for Directional Spectra

The wave measurements using X-band radar follow the electromagnetic theory. Based on the principles of the Bragg scattering mechanism, the electromagnetic waves sent from the radar are backscattered after interaction with the sea surface [4]. Then, the received signals are digitized to form a temporal sequence of backscattered/sea surface roughness images. Using 3-D Fast Fourier Transform (FFT), the time series of radar images were converted to an intensity spectrum. The low-frequency components were removed using a high-pass filter with a cut-off frequency of 0.03 Hz. Using the least-squares method, the depth-averaged currents were estimated, and subsequently, the wave-related components were extracted with a band-pass filter designed using linear-dispersion relation. The modulation effects in the filtered intensity spectrum were corrected using a Modulation Transfer Function (MTF). The processed wave spectra provided by Miros were utilized for the calculations.

The directional spectra were also computed from the wave elevation and wave slopes measured using buoys [2, 9]. The auto- and cross-spectra were estimated from the time series of wave elevation, East-West and North-South wave slopes through Fourier transformation. Welch FFT with a Hanning window was applied to avoid spectral leakage [1]. Subsequently, the directional Fourier coefficients were computed from the auto- and cross-spectra, followed by the estimation of the directional spectrum using MEM. The functions provided by IFREMER (Institut Français de Recherche pour l'Exploitation de la Mer) France were used for calculating the MEM estimate of wave spectra. Let the directional wave spectra obtained using wave radars and buoys be denoted by $S_{\zeta,WR}$ and $S_{\zeta,MEM}$, respectively.

2.3 Vessel hydrodynamic analysis

The actual vessel dimensions are: Overall length, L_{OA} = 36.25 m, length between the perpendiculars, L_{PP} = 33.90 m, Breadth, b = 9.6 m, Draft, T_d= 2.7 m.

The computational analysis was performed using Wamit hydrodynamic code [10] which uses a panel model of the Gunnerus vessel. The hydrostatic and hydrodynamic forces were evaluated with respect to the Body-fixed coordinate system whose origin is at the center of the water plane area CO. However, the IMU was located at a different vessel position, denoted by CM – the center of the measurement axis system, where the measured responses are produced. Using the transformation matrix $\boldsymbol{H}$, the forces and moments at CO were transferred to CM based on the Eqns. (1)−(5). The hydrostatic, hydrodynamic, and transfer function data with a matrix representation are denoted by double overbars $''=''$ and the corresponding data with a vector representation are given by single overbar $'-'$.

$$\overline{\overline{\boldsymbol{M}(\boldsymbol{x})}}^{CM} = \boldsymbol{H}^{-T}\overline{\overline{\boldsymbol{M}}}(\boldsymbol{x})\boldsymbol{H}^{-1} \tag{1}$$

$$\overline{\overline{\boldsymbol{Am}(\omega;\boldsymbol{x})}}^{CM} = \boldsymbol{H}^{-T}\left(\overline{\overline{\boldsymbol{Am}(\omega)}} + \overline{\overline{\boldsymbol{Am}}}^{e}(\boldsymbol{x})\right)\boldsymbol{H}^{-1} \tag{2}$$

$$\overline{\overline{\boldsymbol{B}(\omega;\boldsymbol{x})}}^{CM} = \boldsymbol{H}^{-T}\left(\overline{\overline{\boldsymbol{B}(\omega)}} + \overline{\overline{\boldsymbol{B}^{v}(\boldsymbol{x})}}\right)\boldsymbol{H}^{-1} \tag{3}$$

$$\overline{\overline{\boldsymbol{S}}t}(\boldsymbol{x})^{CM} = \boldsymbol{H}^{-T}\left(\overline{\overline{\boldsymbol{St}(\boldsymbol{x})}} + \overline{\overline{\boldsymbol{St}}}^{e}(\boldsymbol{x})\right)\boldsymbol{H}^{-1} \tag{4}$$

$$\overline{\boldsymbol{F}(\omega,\theta;\boldsymbol{x})}^{CM} = \boldsymbol{H}^{-T}\left(\overline{\boldsymbol{F}(\omega,\theta)} + \overline{\boldsymbol{F}}^{e}(\boldsymbol{x})\right) \tag{5}$$

where $\overline{\overline{\boldsymbol{M}}}^{CM}$, $\overline{\overline{\boldsymbol{Am}(\omega)}}^{CM}$, $\overline{\overline{\boldsymbol{B}(\omega)}}^{CM}$, $\overline{\overline{\boldsymbol{St}}}^{CM}$ are the respective mass, added mass, damping, and stiffness matrices at CM.

$\overline{\boldsymbol{F}(\omega,\theta)}^{CM}$ is a complex excitation force vector at CM. $\overline{\overline{\boldsymbol{M}}}$, $\overline{\overline{\boldsymbol{Am}(\omega)}}$, $\overline{\overline{\boldsymbol{B}(\omega)}}$, $\overline{\overline{\boldsymbol{St}}}$ are the mass, added mass, potential damping and stiffness matrices, respectively computed at CO. $\overline{\boldsymbol{F}(\omega,\theta)}$ is the complex excitation force vector computed at CO. $\overline{\overline{\boldsymbol{Am}}}^{e}$, $\overline{\overline{\boldsymbol{B}}}^{v}$, $\overline{\overline{\boldsymbol{St}}}^{e}$ are the respective external added mass, viscous damping, and additional stiffness matrices defined at CO. $\overline{\boldsymbol{F}}^{e}$ is the external complex excitation coefficient vector at CO. Using the hydrostatic and hydrodynamic data at CM, the wave-to-force transfer function $\left(\overline{\boldsymbol{T}_{\zeta F}} \in \mathbb{C}^{q\times 1}\right)$ and force-to-motion transfer function $(\overline{\overline{\boldsymbol{T}_{FZ}}} \in \mathbb{C}^{q\times q})$ are computed considering the measurement axis system as an inertial frame of reference, given in Eqns. (6) − (7). The index q=1,2,…,6 denotes the six DoF components of vessel motions (Surge, Sway, Heave, Roll, Pitch, Yaw). ζ_a is the wave amplitude. $\mathbb{C}$ is used for representing complex numbers.

$$\overline{\overline{\boldsymbol{T}_{FZ}}}(\omega;\boldsymbol{x}) = \left((-\omega^2\left(\overline{\overline{\boldsymbol{M}}}(\boldsymbol{x})^{CM} + \overline{\overline{\boldsymbol{Am}(\omega;\boldsymbol{x})}}^{CM}\right) + i\omega(\overline{\overline{\boldsymbol{B}(\omega;\boldsymbol{x})}}^{CM}) + \overline{\overline{\boldsymbol{St}}}(\boldsymbol{x})^{CM})\right)^{-1} \tag{6}$$

$$\overline{\boldsymbol{T}_{\zeta F}}(\omega,\theta;\boldsymbol{x}) = \frac{\overline{\boldsymbol{F}(\omega,\theta;\boldsymbol{x})}^{CM}}{\zeta_a} \tag{7}$$

where ω is the wave frequency, θ denotes the relative directions, and system variables are given by $\boldsymbol{x} = \{(x_\alpha), \alpha = 1,2,\dots,\mathcal{M}\}$. $\mathcal{M}$ is the number of input variables. The complex motion transfer function, $\overline{\boldsymbol{T}_{\zeta Z}} \in \mathbb{C}^{q\times 1}$, is defined as the product of $\overline{\overline{\boldsymbol{T}_{FZ}}}$ and $\overline{\boldsymbol{T}_{\zeta F}}$. $\overline{\boldsymbol{T}_{\zeta Z}}$ relates the wave elevation ζ at a reference point to the motion response $\overline{\boldsymbol{Z}} = \{(Z_q)\}$.

$$\overline{\boldsymbol{T}_{\zeta Z}}(\omega,\theta;\boldsymbol{x}) = \overline{\overline{\boldsymbol{T}_{FZ}}}(\omega;\boldsymbol{x})\,\overline{\boldsymbol{T}_{\zeta F}}(\omega,\theta;\boldsymbol{x}) \tag{8}$$

The squared amplitude values of the motion transfer function, $\left\{T_{\zeta Z_q}T^*_{\zeta Z_r} = \left|T_{\zeta Z_{q,r}}\right|^2, \forall q = r, r = 1,2,\dots,6\right\}$, are then applied to compute the auto-response spectrum ($S_{Z_{qq}}(\omega,\theta;\boldsymbol{x}) \in \mathbb{R}^{+\omega\times\theta}$), which is expressed as

$$S_{Z_{qq}}(\omega,\theta;\boldsymbol{x}) = S_\zeta(\omega,\theta)\left|T_{\zeta Z_{q,r}}(\omega,\theta;\boldsymbol{x})\right|^2,\ r{=}q \tag{9}$$

Integration across the directional axis of $S_{Z_{qq}}(\omega,\theta;\boldsymbol{x})$ gives the response spectrum as a function of frequency alone $S_{Z_{qq}}(\omega;\boldsymbol{x})$, which is the simulated Quantity of Interest (QoI). Similarly, the measured response QoI $S_{Z_{qq,MT}}$, were obtained by performing 1-D Welch FFT [11] on the measured response time series. The time series was segregated into segments and the Parzen window was applied for the smoothing.

2.4 Model Tuning

The computational model was tuned by minimizing the error between the measured and simulated spectra in an optimization framework.

$$minimize\ f(\boldsymbol{x}),\ \ \forall\, \boldsymbol{x} \in \mathbb{R}^{\mathcal{M}}$$

$\boldsymbol{x}$ is a vector denoting the variables from $\mathcal{M}$ dimensional space and $f(\boldsymbol{x})$ represents the objective function. Bounded constraints were adopted for each variable x_α, with lo_α and up_α denoting the variable's lower and upper limits. Consequently, the restricted search space Ω becomes

$$\boldsymbol{\Omega} = \{\boldsymbol{x} | lo_\alpha \le x_\alpha \le up_\alpha\} \subset \mathbb{R}^{\mathcal{M}}$$

The objective function to minimize the error between the measured and simulated spectral density is formulated as

$$f_{\boldsymbol{\Omega},SPEC}(\boldsymbol{x}) = \sum_q \left(\sum_{h=1}^{N_\omega}\left|(w_q(S_{Z_{qq,MT}}(\omega_h;\boldsymbol{x})\Delta\omega) - w_q(S_{Z_{qq}}(\omega_h;\boldsymbol{x})\Delta\omega))\right|\right) \tag{10}$$

The weight term w_q can be set to zero for modes not included in the tuning. The objective function shown in Eq. (10) was minimized using a derivative-free optimization called Mesh Adaptive Direct Search (MADS) [12].

2.5 Sensitivity of the Objective function

The sensitivity of the objective function $f_{\boldsymbol{\Omega},SPEC}$ to parametric variation was studied using the Variance-based indices called Sobol' indices [13] to identify the influential variables. It is presumed that on satisfying certain conditions proposed by Sobol' [13], the variance of $f_{\boldsymbol{\Omega},SPEC}(\boldsymbol{X})$ can be decomposed in the form given in Eq. (11). Letter '$\boldsymbol{X}$' is used to denote the system variables in this section, as they are considered as random variables associated with a probability measure.

$$V = V[f_{\boldsymbol{\Omega},SPEC}(\boldsymbol{X})] = \sum_{\alpha=1}^{M} V_\alpha + \sum_{1\le\alpha<\beta\le\mathcal{M}} V_{\alpha\beta} + \cdots + V_{1\dots\mathcal{M}} \tag{11}$$

Here, $V_\alpha = V\left[\mathbb{E}\left[f_{\boldsymbol{\Omega},SPEC}(\boldsymbol{X})|X_\alpha\right]\right]$, $V_{\alpha\beta} = V\left[\mathbb{E}\left[f_{\boldsymbol{\Omega},SPEC}(\boldsymbol{X})|X_\alpha,X_\beta\right]\right] - V_\alpha - V_\beta$. $\mathbb{E}\left[f_{\boldsymbol{\Omega},SPEC}(\boldsymbol{X})|X_\alpha\right]$ and $\mathbb{E}\left[f_{\boldsymbol{\Omega},SPEC}(\boldsymbol{X})|X_\alpha,X_\beta\right]$ are the conditional expectations of $f_{\boldsymbol{\Omega},SPEC}$ with respect to each input variable X_α and any two combinations of input variables X_α X_β, respectively. The sensitivity is derived by dividing individual variance terms in Eq. (11) by the total variance V

$$\sum_{\alpha=1}^{\mathcal{M}} SI_\alpha + \sum_{1\le\alpha<\beta\le\mathcal{M}} SI_{\alpha\beta} + \cdots + SI_{1\dots\mathcal{M}} = 1 \tag{12}$$

SI_α denotes the first-order indices that analyze the effect of each uncertain parameter on the response. The second-order indices, $SI_{\alpha\beta}$, reports the effects on the responses because of interaction between two variables. There are also higher-order Sobol' indices like 3rd order, 4th order, and so on in relation to the number of input variables. The total sensitivity indices are

the composition of the first-order indices and all other interaction terms in Eq. (12). Instead of computing all the higher-order Sobol' indices, which is extremely challenging, and then calculating the total sensitivity indices; a simple relation in Eq. (13) can be employed to estimate the total sensitivity indices efficiently. $\boldsymbol{X}_{\sim\alpha}$ represents all input variables other than X_α.

$$SI_\alpha^T = 1 - \frac{V\left[\mathbb{E}[f_{\boldsymbol{\Omega},SPEC}(\boldsymbol{X})|\boldsymbol{X}_{\sim\alpha}]\right]}{V[f_{\boldsymbol{\Omega},SPEC}(\boldsymbol{X})]} \quad (13)$$

A method called Polynomial Chaos Expansion (PCE) was used to construct a response surrogate for the objective function. Subsequently, the Sobol' indices were estimated from the polynomial coefficients of the surrogate [14]. The detailed estimation procedures are given in [6, 15]. The influential variables identified using the sensitivity study are applied for model tuning.

3. METHODOLOGY

Almost 31 vessel system parameters, representing the vessel loading conditions and unmodelled physics, were considered for the uncertainty analysis. For instance, the CoG, inertia, and additional stiffness terms account for the changes in the vessel's operational conditions. On the other hand, the viscous damping coefficients, non-linear added mass, and excitation variables were included to represent the unmodelled physics in the potential flow theory. The real and imaginary components are considered separately as random variables to solve the complex external excitation forces and moments. The parameters for capturing the unmodelled physics could be sea state-dependent. Further, both the operational and unmodelled physical parameters might vary with respect to the changes in vessel draft conditions. The variables were supplied to the optimization routine in a bounded format, therefore, Uniform distributions with statistical independence were assumed for the system variables in the sensitivity study.

The flowchart shown in Fig. 2 illustrates the model tuning methodology.

a) The measured directional spectra, S_ζ were obtained from the wave radars and buoys as per the techniques in Sec. 2.2. The spectra represent the true environmental conditions at the site.
b) The response time series $\mathcal{Z}_q(t)$ was deducted with its mean ($\mathbb{E}[\mathcal{Z}_q]$) to remove any static patterns, and high-pass filtered with a cut-off frequency of 0.035 Hz to neglect any low-frequency responses. Only the measured responses corresponding to wave frequencies were considered for tuning.
c) Eq. (10) was evaluated keeping the S_ζ,vessel heading (V_θ), mean wave direction (θ_m) fixed and varying the system parameters probabilistically as per the distributions listed in Table 2.
d) Then, a response surrogate $f_{\boldsymbol{\Omega},SPEC}^{PC}$ was constructed and PCE-Sobol' indices were estimated to analyze the sensitivity of the objective function to parametric variation.
e) Influential parameters ($\boldsymbol{x}_{in} \subset \boldsymbol{x}$) were classified whose Sobol' index value is $\geq 4\%$. Parameters with index values below this threshold limit were considered non-influential ($\boldsymbol{x}_{nin} \subset \boldsymbol{x}$).

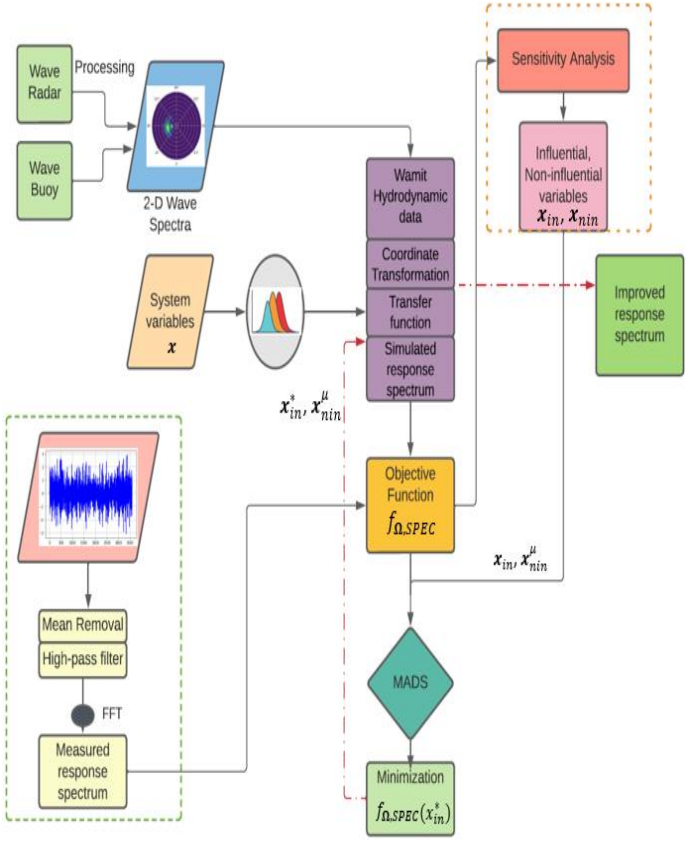

FIGURE 2: FLOW OF WORK FOR THE MODEL TUNING PROCEDURE.

f) Only $\boldsymbol{x}_{in}$ were applied in the optimization routine (within the given bounds), and the mean values ($\boldsymbol{x}_{in}^\mu$) were specified as the initial start points to initiate the optimization. Non-influential parameters were kept fixed during the optimization. A deterministic value, i.e., mean value ($\boldsymbol{x}_{nin}^\mu$), was applied.
g) The minimization of the error between the measurements and simulations provides optimum values of the influential parameters denoted by $\boldsymbol{x}_{in}^*$.
h) Minimization of $f_{\boldsymbol{\Omega},SPEC}$ was performed with a derivative-free optimization called Mesh Adaptive Direct Search (MADS) [12]. A Python interface to the Nonlinear Mesh Adaptive Direct Search (NOMAD)

c++ library was used [16]. $\boldsymbol{x}_{in}^{*}$ can be applied for computing the improved simulations $S_{Z_{qq}}^{+}$.

TABLE 2: LIST OF SYSTEM PARAMETERS WITH THEIR UNCERTAINTY RANGES. THEIR ACRONYM IS GIVEN IN THE NOMENCLATURE SECTION.

System Parameters	Uncertainty Range	
$Xcg(m)$	Uniform($lo_1 = -3.78$,	$up_1 = 0.22$)
$Ycg(m)$	Uniform($lo_2 = -1.0$,	$up_2 = 1.0$)
$Zcg(m)$	Uniform($lo_3 = 0.4$,	$up_3 = 1.0$)
$M(kg)$	Uniform($lo_4 = M - 5\%\, M$,	$up_4 = M + 5\%\, M$)
$I_{44}(kgm^2)$	Uniform($lo_5 = I_{44} - 5\%\, I_{44}$,	$up_5 = I_{44} + 5\%\, I_{44}$)
$I_{55}(kgm^2)$	Uniform($lo_6 = I_{55} - 5\%\, I_{55}$,	$up_6 = I_{55} + 5\%\, I_{55}$)
$I_{66}(kgm^2)$	Uniform($lo_7 = I_{66} - 5\%\, I_{66}$,	$up_7 = I_{66} + 5\%\, I_{66}$)
$B_{33}^{v}(\frac{kg}{s})$	Uniform($lo_8 = 0\%\, B_{33,cr}^{v}$,	$up_8 = 15\%\, B_{33,cr}^{v}$)
$B_{44}^{v}(kg\frac{m^2}{s})$	Uniform($lo_9 = 2\%\, B_{44,cr}^{v}$,	$up_9 = 25\%\, B_{44,cr}^{v}$)
$B_{55}^{v}(kg\frac{m^2}{s})$	Uniform($lo_{10} = 0\%\, B_{55,cr}^{v}$,	$up_{10} = 15\% B_{55,cr}^{v}$)
$St_{33}^{e}(KN/m)$	Uniform($lo_{11} = -5441.951$	$up_{11} = 5441.951$)
$St_{44}^{e}(KNm/rad)$	Uniform($lo_{12} = -5440.96$,	$up_{12} = 5440.96$)
$St_{55}^{e}(KNm/rad)$	Uniform($lo_{13} = -10881.63$,	$up_{13} = 10881.63$)
$Am_{11}^{e}(tonnes)$	Uniform($lo_{14} = -500$,	$up_{14} = 500$)
$Am_{22}^{e}(tonnes)$	Uniform($lo_{15} = -5000$,	$up_{15} = 5000$)
$Am_{33}^{e}(tonnes)$	Uniform($lo_{16} = -20000$,	$up_{16} = 20000$)
$Am_{44}^{e}(tonnes\ m^2)$	Uniform($lo_{17} = -25000$,	$up_{17} = 25000$)
$Am_{55}^{e}(tonnes\ m^2)$	Uniform($lo_{18} = -10 \times 10^5$,	$up_{18} = 10 \times 10^5$)
$Am_{66}^{e}(tonnes\ m^2)$	Uniform($lo_{19} = -3 \times 10^5$,	$up_{19} = 10 \times 10^5$)
$Fr_1^{e}(MN)$	Uniform($lo_{20} = -2.0$,	$up_{20} = 2.0$)
$Fi_1^{e}(MN)$	Uniform($lo_{21} = -3.0$,	$up_{21} = 3.0$)
$Fr_2^{e}(MN)$	Uniform($lo_{22} = -2.5$,	$up_{22} = 2.5$)
$Fi_2^{e}(MN)$	Uniform($lo_{23} = -10$,	$up_{23} = 10$)
$Fr_3^{e}(MN)$	Uniform($lo_{24} = -30$,	$up_{24} = 30$)
$Fi_3^{e}(MN)$	Uniform($lo_{25} = -15$,	$up_{25} = 15$)
$Fr_4^{e}(MNm)$	Uniform($lo_{26} = -8.5$,	$up_{26} = 8.5$)
$Fi_4^{e}(MNm)$	Uniform($lo_{27} = -2.5$,	$up_{27} = 2.5$)
$Fr_5^{e}\ (MNm)$	Uniform($lo_{28} = -90$,	$up_{28} = 90$)
$Fi_5^{e}\ (MNm)$	Uniform($lo_{29} = -200$,	$up_{29} = 200$)
$Fr_6^{e}\ (MNm)$	Uniform($lo_{30} = -60$,	$up_{30} = 60$)
$Fi_6^{e}\ (MNm)$	Uniform($lo_{31} = -10$,	$up_{31} = 10$)

4. RESULTS AND DISCUSSION

4.1 Directional Spectra from Buoy and Wave Radar

Fig. 3 shows the directional spectra $S_{\zeta,WR}$ and $S_{\zeta,MEM}$ in the meteorological axis system for the time period between 08:00 - 08:38 UTC on 03/04/2022. The swell was arriving from the open ocean to Breisundet and the wind waves were generated by winds blowing from Sulafjorden. Therefore, the wave spectrum was bi-modal in nature. From the buoy-based directional spectra, it appears that the directions of wind sea and swell are not considerably different. This is because Breisundet is a narrow strait whose geometry influences the directions of the different sea systems to be aligned along the strait's axis. Between, 0.5-0.8 rad/s, the peak due to swell could be seen in both radar-based ($S_{\zeta,WR}$) and buoy-based ($S_{\zeta,MEM}$) spectra. Then, the $S_{\zeta,WR}$ shows a wind peak at frequencies between 0.8-1.25 rad/s. However, $S_{\zeta,MEM}$, displays two more peaks in between the frequency range 0.8-1.25 rad/s in addition to the swell peak. In order to classify the peaks, the phase velocity (C_p=$\frac{g}{\omega_p}$, ω_p- peak frequency) of the peaks are compared with the locally buoy-measured wind speed. The phase velocities of three peaks are 13.246 $\frac{m}{s}$, 9.117 $\frac{m}{s}$, and 7.948 $\frac{m}{s}$ corresponding to the frequencies 0.74, 1.076, 1.234 $\frac{rad}{s}$, respectively. The measured wind velocity is 10.02 $\frac{m}{s}$. The peak phase velocity greater than the wind speed corresponds to the swell peak, while the phase velocities lesser than the wind speed correspond to wind sea induced peaks. It is possible to have multiple wind sea peaks, i.e., one/two old and young wind seas due to different fetches, which is a characteristic of Breisundet. The magnitude of $S_{\zeta,WR}$ is slightly lesser than $S_{\zeta,MEM}$, however, there are considerable differences in the directional spread. The spectral energy of $S_{\zeta,WR}$ extends into more directional bins, while the energy of $S_{\zeta,MEM}$ extends into the high-frequency regions. $S_{\zeta,WR}$ has uncertainties related to correcting different modulation mechanisms and scaling effects.

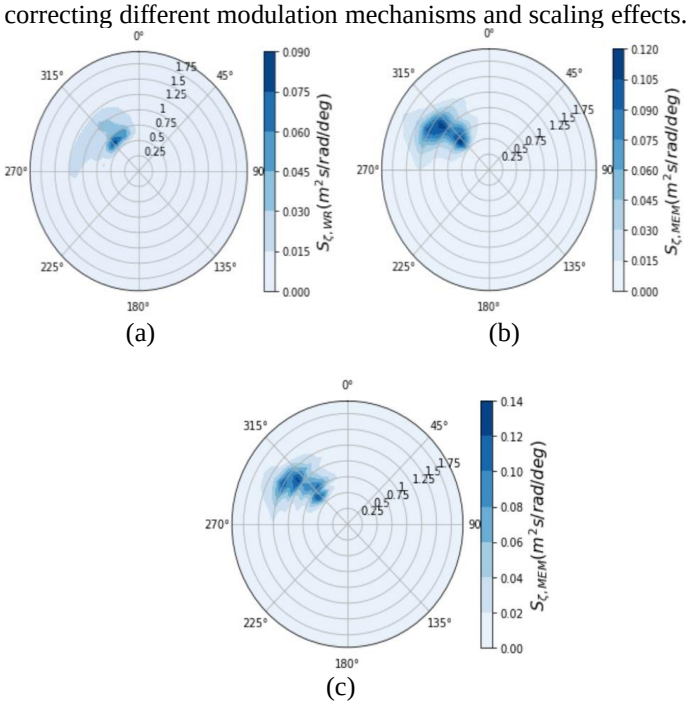

FIGURE 3: COMPARISON BETWEEN THE DIRECTIONAL SPECTRA OBTAINED FROM A) WAVE RADAR IMAGES B) APPLICATION OF MEM ON WAVE BUOY DATA WITH A SEGMENT LENGTH OF 128 ADOPTED IN FFT C) MEM ON WAVE BUOY DATA WITH A SEGMENT LENGTH OF 256 ADOPTED IN FFT. THE DATA ON 03/04/22, 08:00-08:38 UTC WAS USED FOR PLOTTING.

The directional spread in $S_{\zeta,MEM}$ must not be interpreted as true spread due to the uncertainties in the application of smoothing window while estimating 1-D auto- and cross-spectra from the time series. Subsequently, these uncertainties are reflected in the directional Fourier coefficients as well. The

choice of window length considerably affects the spectral magnitude and spread. Fig. 3 b) and c) show that the magnitude increases, while the directional spread looks coarse and shrinks with increasing segment length. Since it is not known beforehand which measurement technique is closest to the truth, the model tuning was performed using both wave spectra and the results are presented in Sec. 4.3.

4.2 Sensitivity Results

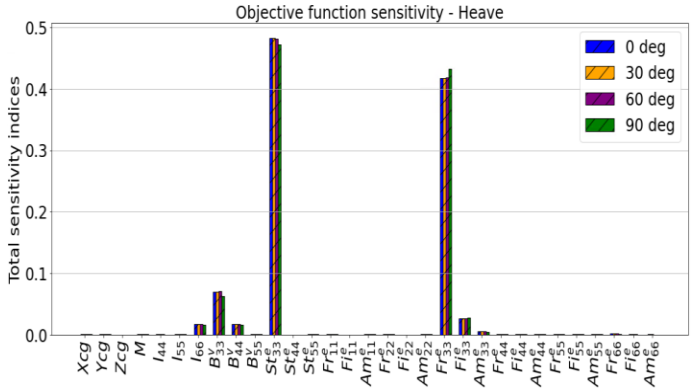

(a)

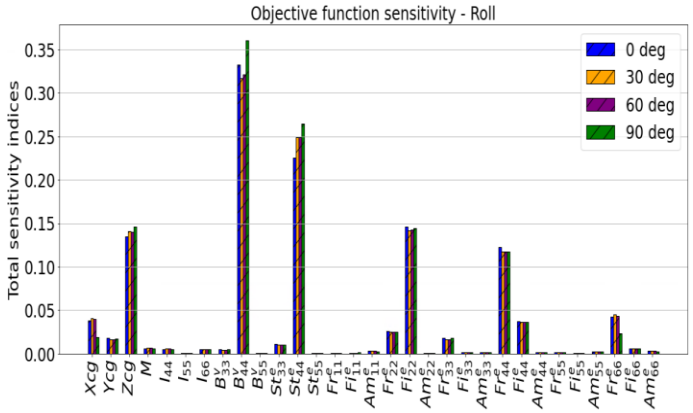

(b)

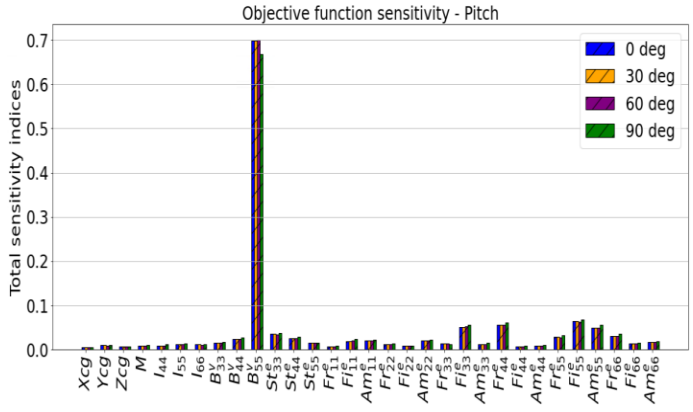

(c)

FIGURE 4: TOTAL SENSITIVITY OF A) HEAVE, B) ROLL AND C) PITCH OBJECTIVE FUNCTION TO PARAMETRIC VARIATION CONSIDERING 31 RANDOM SYSTEM PARAMETERS

Using PCE-Sobol' indices, the sensitivity of the a) Heave, b) Roll, and Pitch objective functions due to system uncertainties were analyzed for the 4 relative headings considered. Their total sensitivity indices are reported in Fig. 4 a), b), and c). The sensitivity of each mode in $f_{\boldsymbol{\Omega},SPEC}(\boldsymbol{x})$ in Eq. (10)**,** was analysed separately by setting the weights of other modes to zero. B^v_{33}**,** St^e_{33}, and the real part of the external heave excitation force (Fr^e_{33}) are contributing almost 7%, 48%, and 43%, respectively to the total variability of the heave objective function. Similarly, changes in the viscous pitch damping contribute to around 70% of the variations in the pitch error function. The pitch added mass, Fr^e_{44}, Fi^e_{33}, Fi^e_{55} are exceeding the set threshold limit and therefore considered influential, whereas many other non-influential variables were disregarded. The effects due to the external pitch stiffness term seem negligible, as the considered parameter variation range is small. However, the results might differ when having a larger uncertainty range. Almost 7 parameters $\{Xcg,Zcg,B^v_{44},St^e_{44},Fr^e_{44},Fr^e_{66},Fi^e_{22}\}$ seem to influence the roll function. The Zcg, B^v_{44}**,** and St^e_{44}, respectively are responsible for around 15%, 35%, and 25% variation in the roll error function. The external imaginary and real excitation components of sway and roll, respectively are triggering 14% and 12% of the roll error variation.

Overall, when considering the three modes together, the following variables were regarded as influential $\boldsymbol{x}_{in}$=$\{Xcg,Zcg,B^v_{33},B^v_{44},B^v_{55},St^e_{33},St^e_{44},Fr^e_{33},Fr^e_{44},Fr^e_{66},Fi^e_{22},Fi^e_{33},Fi^e_{55},Am^e_{55}\}$, and tuned together by minimizing the objective function $f_{\Omega,SPEC}(\boldsymbol{x})$. The values of sensitivity indices do not vary much with respect to changes in relative headings. Only for the beam sea, a few parameters (Xcg, B^v_{44}, St^e_{44}) slightly exhibit some variations.

4.3 Computational model tuning results

At each relative heading, heave, roll, and pitch motions were measured using an IMU, and simultaneous wave measurements from wave radar and buoy were also available. The wave spectra derived from both in-situ techniques were applied in model tuning and the corresponding response results are compared with the measurements in Figs. 5,6,7 for heave, roll and pitch modes, respectively. The segment length adopted for the FFT computations in MEM is 256. In Fig. 5, the first peak corresponds to the heave resonance while the second peak is due to the excitation forces. The swell induces the resonance peak, and the wind waves cause the excitation peak. The tuned heave results using both wave spectra agree well with the measurements. Still, there are some discrepancies at the second peak. The results based on the buoy directional spectrum can better quantify the oscillations in the second peak compared to the results from the wave radar spectrum, especially in Fig. 5 b)**.** The contribution from the excitation forces is larger in heave, which was also reflected in the sensitivity indices of the heave error function. The roll results in Fig. 6 indicate that

there is only a single peak in the response spectrum governed by the roll resonance behavior. The roll natural period (~5.4 s) is closer to the wind wave period. The tuned roll simulations exhibit superior agreement with the measurements. For roll, the responses when the relative heading is 0 deg are small, while the responses are ten-fold higher in the 90 deg case. The H_s also increased from 1.1 m at 07:00 AM to 1.4 m at 10:00 AM, which is quite higher for a 30 m vessel. Based on visual inspection, for roll and pitch, the tuned simulations corresponding to the wave spectrum estimated from the buoy measurements produce slightly better response results than the tuning with radar-based wave spectrum. Since the mean wave directions of wind seas and swell are not completely different, the directional spectra estimated using MEM can better reflect the wave conditions at the site for the considered cases. However, in Fig. 7 d), the discrepancy in the high-frequency tail could be observed for the pitch response simulated using the buoy spectrum. This deviation is due to the presence of wave energy in the high-frequency region in the buoy spectrum.

Only the influential variables identified in Sec. 4.2 were tuned. Low sensitivity indices for variables indicate that they possess low eigenvalues. Consequently, such variables tend to make the objective function space non-unique when all of them are included for tuning. Due to the existence of non-unique solutions, the low-sensitive variables are allowed to take any values within their uncertainty range during the optimization, while at the same time, the results are not modified drastically. It follows that even if the resulting responses are accurate, the optimized parameter estimates may be biased. Therefore, it is important to neglect such variables in the optimization.

From the viewpoint of an offshore vessel performing an offshore operation, the vessel model could be calibrated before the initiation of the operations. Further, when there are significant changes in the operational conditions, for instance, a heavy mass shift during the crane movement, variations in ballast, fuel tank conditions, and moon pool operations influences the CoG and stiffness parameters. Then those operational parameters must be tuned to account for the changes. While, the sea state-dependent parameters might vary considerably during harsh sea states, and need tuning in such cases. Further, the change of draft might also cause variation to both operational and sea state-dependent parameters.

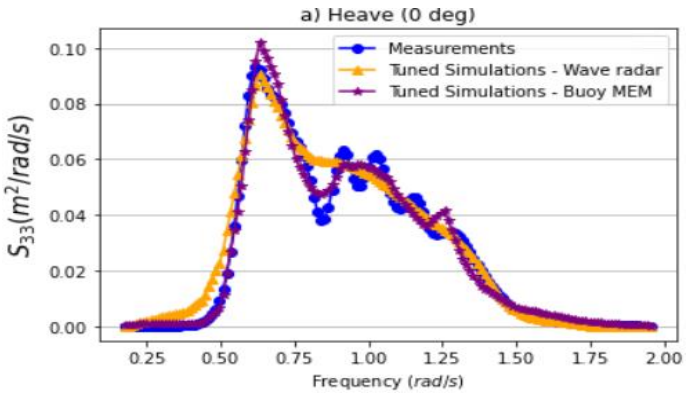

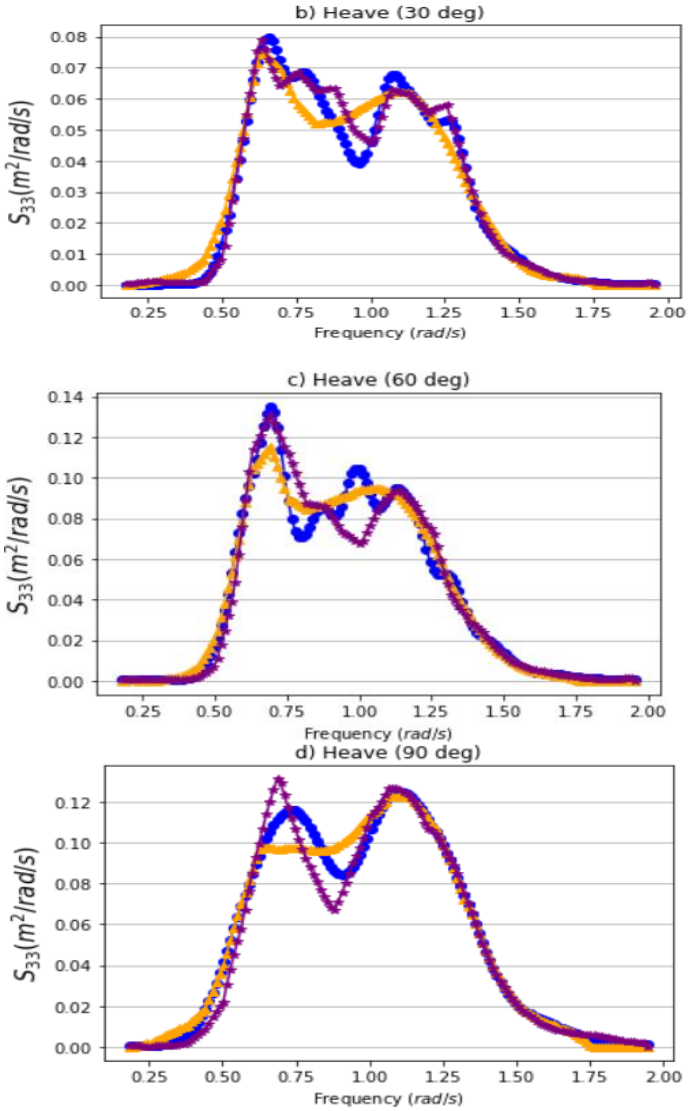

FIGURE 5: A),B),C),D) SIMULATED HEAVE SPECTRA TUNED USING THE WAVE SPECTRA FROM WAVE RADARS AND WAVE BUOYS ARE COMPARED WITH THE MEASURED HEAVE SPECTRUM FOR 4 DIFFERENT HEADINGS

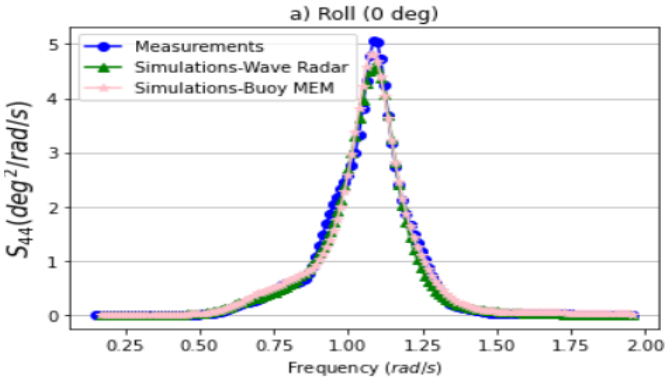

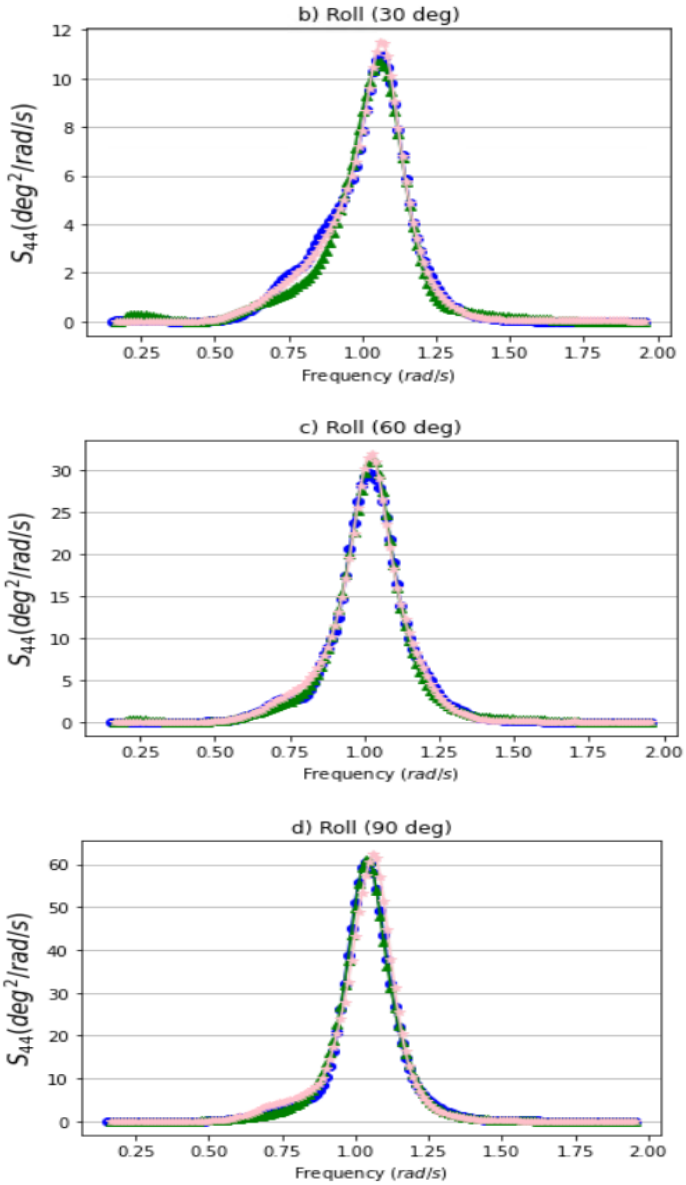

FIGURE 6: A),B),C),D) SIMULATED ROLL SPECTRA TUNED USING THE WAVE SPECTRA FROM WAVE RADARS AND WAVE BUOYS ARE COMPARED WITH THE MEASURED ROLL SPECTRUM FOR 4 DIFFERENT HEADINGS.

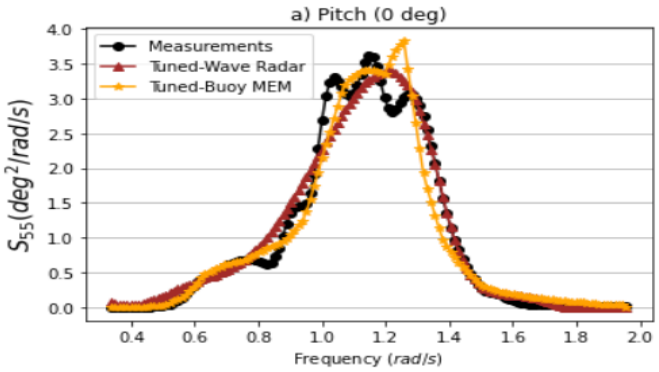

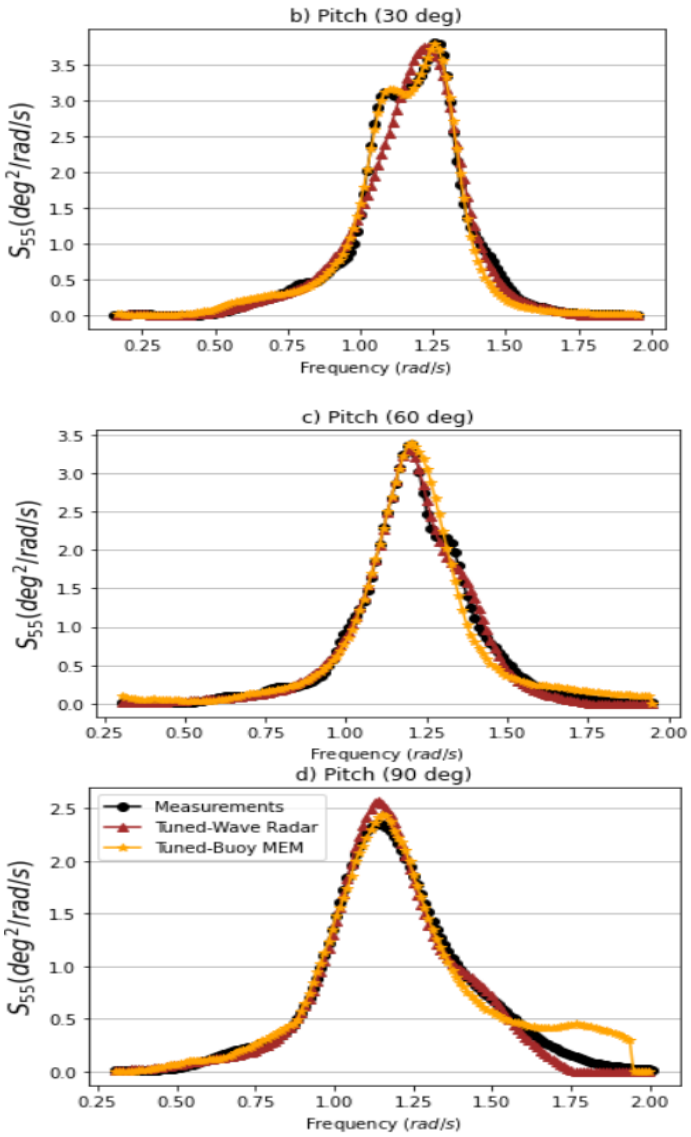

FIGURE 7: A),B),C),D) SIMULATED PITCH SPECTRA TUNED USING THE WAVE SPECTRA FROM WAVE RADARS AND WAVE BUOYS ARE COMPARED AGAINST THE MEASURED PITCH SPECTRUM FOR 4 DIFFERENT HEADINGS

5. CONCLUSION AND FUTURE WORK

For usage in onboard decision support systems of offshore vessels, a real-time computational model tuning procedure was presented and validated in this study. The method utilizes wave conditions measured using in-situ techniques like wave buoys and X-band wave radars, and the vessel's own IMU measurements to tune the vessel system parameters.

The sensitivity of the objective function to parametric variation involving 31 parameters indicated that only 14 of them were influential. From the operational dependent parameter category, the CoG and external stiffness variables appear to be crucial for vessel rolling. The respective additional viscous damping coefficients impart considerable variation to the roll and pitch modes. The real and imaginary components of external excitation forces have uneven influences, mostly, the

real components are inducing more variations to the error function than the imaginary components. The optimized estimates of the influential parameters were obtained using MADS optimization. Tuning only the influential parameters can greatly save computational time with negligible loss of accuracy.

The model tuning using the directional spectra from Buoys resolved some sharp peaks in the response spectra, which could not be achieved when tuning with spectra from wave radars, as $S_{\zeta,WR}$ could not capture the different partitions of the wind sea. The presence of energy in the high-frequency regions of the buoy spectrum caused slight errors. In general, the tuning results can further be improved with a properly chosen segment length while applying the FFT to the wave elevation and slope time series of buoy measurements. The wave buoy data may not be available in real-time due to the time required for processing the data and they are available only at sparse spatial locations. On the other hand, wave radar data are easily available in real-time and can be installed in the vessels. Therefore, more research should focus on retrieving accurate wave conditions from radar images.

The model is tuned by minimizing the difference between the measured and the simulated response spectra. The measured spectra possess some random errors when applying FFT. The spectrum at each frequency is a Chi-square distributed variable with 2-(Degrees of Freedom)DOF(χ_2^2). The sampling distribution of the complete spectrum is χ_{2L}^2, L is the number of segments applied in FFT. Due to this spectral variance/random errors, the optimized parameter estimates might not be the true estimates, so a confidence interval must be derived for the parameters which is the subject of further study.

ACKNOWLEDGEMENTS

This work was made possible through the Centre for Research-based Innovation MOVE, financially supported by the Research Council of Norway, NFR project no. 237929 and the consortium partners, http://www.ntnu.edu/move. Mickael Accensi from IFREMER is thanked for providing functions MEM estimation. Wim Lavrijsen, AIDE-QC, Lawrence Berkely National Laboratory, is sincerely thanked for providing the Python wheels for Nomad 4 c++ library.

REFERENCES

[1] National Data Buoy Center, "Non-Directional and Directional Wave Data Analysis Procedures," National Oceanic and Atmospheric Organization, Louisiana, 1996.

[2] A. Lygre and H. E. Krogstad, "Maximum Entropy Estimation of the Directional Distribution in Ocean Wave Spectra," *Journal of Physical Oceanography,* vol. 16, no. 12, pp. 2052-2060, 1986.

[3] H. E. Krogstad and S. S. Barstow, "Satellite wave measurements for coastal engineering applications," *Coastal Engineering,* no. 37, pp. 283-307, 1999.

[4] S. Støle-Hentschel, J. Seeman, J. C. N. Borge and K. Trulsen, "Consistency between Sea Surface Reconstructions from Nautical X-band Radar Doppler and Amplitude Measurements," *Journal of Atmospheric and Oceanic Technology,* 2018.

[5] L. R. Wyatt, "Measuring the ocean wave directional spectrum 'First Five' with HF radar," *Ocean Dynamics*, no. 69, pp. 123-144, 2018.

[6] G. Radhakrishnan, X. Han, S. Sævik, Z. Gao and B. J. Leira, "System Uncertainty Effects on the Wave Frequency Response of Floating Vessel Based on Polynomial Chaos Expansion, OMAE2021-62542," in *Proceedings of the ASME 2021 40th International Conference on Ocean, Offshore and Arctic Engineering*, Virtual, Online, 2021.

[7] G. Radhakrishnan, B. J. Leira, Z. Gao, S. Sævik and A. Gomola, "Motion Response Prediction of Marine Vessels Based on Hydrodynamic Models Updated Through On-Site Measurements," in *Proceedings of the ASME 2022 41st International Conference on Ocean, Offshore and Arctic Engineering* , Hamburg, Germany, 2022.

[8] B. R. Furevik, L. Lønseth, A. L. Borg, V. Neshaug and M. Gausen, "Oceanographic observations for the Coastal Highway E39 project in Mid-Norway," The Norwegian Meteorological Institute, 2016.

[9] S. F. Barstow and H. E. Krogstad, "General analysis of directional ocean wave data from heave/pitch/roll buoys," *Modeling, Identification and Control,* vol. 5, no. 1, pp. 47-70, 1984.

[10] WAMIT INC, "WAMIT, The state of the art in wave interaction analysis," Massachusetts Institute of Technology, Chestnut Hill, MA, 2014.

[11] P. D. Welch, "The Use of Fast Fourier Transform for the Estimation of Power Spectra: A Method Based on Time Averaging Over Short, Modified Periodograms," *IEEE Transactions on Audio and ElectroAcoustics,* pp. 70-73, 1967.

[12] J. Charles Audet & J.E. Dennis, "Mesh Adaptive Direct Search Algorithms for Constrained Optimization," *SIAM Journal of Optimization,* vol. 18, no. 4, pp. 188-217, 2008.

[13] A. Saltelli, M. Ratto, T. Andres, F. Campolongo, J. Cariboni, D. Gatelli and S. T. M. Saisana, Global Sensitivity Analysis. The Primer, Chichester; West Sussex: John Wiley & Sons, Ltd, 2008.

[14] C. Lataniotis, D. Wicaksono, S. Marelli and B. Sudret, "UQLab, User Manual," Chair of Risk, Safety and Uncertainty Quantification, ETHZ, Zurich, Switzerland, 2019.

[15] B. Sudret, "Global sensitivity analysis using polynomial chaos expansions," *Reliability Engineering & System Safety,* pp. 964-979, 2007.

[16] W. Lavrijsen, "Scikit-Quant," 2021.